DOI: 10.1002/ejic.200701033

Solid-State Organic/Inorganic Hybrid Solar Cells Based on Poly(octylthiophene) and Dye-Sensitized Nanobrookite and Nanoanatase TiO_2 Electrodes

Emmanuelle Lancelle-Beltran,*[a] Philippe Prené,[a] Christophe Boscher,[a] Philippe Belleville,[a] Pierrick Buvat,[a] Sébastien Lambert,[a] François Guillet,[a] Corinne Marcel,[a] and Clément Sanchez[b]

Keywords: Solar cells / TiO_2 nanoparticles / Brookite / Photovoltaic / DSSC

The performance of solid-state hybrid dye-sensitized solar cells (DSSC), based on polythiophene polymers as hole-transporting materials, have been compared by varying TiO_2 mesoporous n-semiconductor film microstruture parameters such as the crystalline phase (brookite and anatase), initial crystallite size and sintering temperature conditions. For both crystalline phases a rise in the TiO_2 mesoporous film curing temperature from 450 °C to 600 °C produces a twofold increase in the energy conversion efficiency leading to a significant current density improvement. When using the same solar-cell preparation process and a 500-nm-thick photoactive layer, the cells made up of brookite and anatase mesoporous materials give a reproducible solar energy conversion efficiency that reaches 0.48 % and 0.74 %, respectively (at standard AM 1.5).

Introduction

Alternative energy sources are of increasing interest because of the diminishing petroleum reserve and are needed to replace the environmentally damaging fossil fuels. Solar power is obviously one of the most attractive solutions. Up to now, the main photovoltaic (PV) devices are based on P-N silicon solid-state junctions and expensive technology ensues directly from the development of the semiconductor industry. In this situation, a challenging new generation of solar cells is merging in which the P-N junction photovoltaic device is replaced by a system of interpenetrating networks of nanocrystalline oxide and conducting electrolytes. The so-called dye-sensitized solar cells (DSSC) are a technically and economically viable alternative to the conventional silicon photovoltaic devices because of easy fabrication and low cost.[1] They use a mesoporous TiO_2 layer as a semiconductor layer, a ruthenium-based complex as a dye and a redox couple-containing liquid as an electrolyte. For such liquid solar cells a 10% higher energy conversion efficiency is achieved under standard white solar-light illumination (1000 $W m^{-2}$, i.e. standard AM 1.5) with good durability.[2] But, to the best of our knowledge, this has not provided any commercial applications because of technological issues induced by the use of a highly corrosive liquid electrolyte (cell sealing, handling, maintenance and device production). The all-solid-state dye-sensitized solar cells have been developed by replacing the liquid electrolyte with ionically conducting gels,[3] or inorganic *p*-type materials such as CuI and CuSCN,[4] or organic hole-conductive polymers such as triphenyldiamine, polypyrole or polythiophene.[5,6] This third generation of hybrid organic–inorganic PV cells is very promising with attractive overall efficiencies.[5,7] Because of the potential development of low cost photovoltaic cells deposited onto large-size and flexible substrates, such all-solid-state dye-sensitized photovoltaic devices are currently under intensive investigation.[8]

The TiO_2 layer plays two key roles in the all-solid dye-sensitized solar cells. The main purpose of the inorganic semiconductor is to accept electrons from the light absorption excited-state dye. The second one is to present an extremely high surface area in order to improve the cell energy conversion efficiency. The polymorphs of TiO_2, rutile, anatase and brookite exhibit specific physical properties, bandgaps and electronic surface states.[9] These three polymorphs can be synthesized by thermolysis of titanium tetrachloride ($TiCl_4$) in an aqueous medium, and the precipitation conditions (acidity, nature of anions, ionic strength, titanium concentration) enable the control of the crystalline structure, size and particle morphology.[10] Spheroidal nanoanatase platelets of pure nanobrookite and rutile with different shapes (needle, rod or platelets) can be prepared

[a] CEA-Le Ripault,
B. P. 16, 37260 Monts, France
Fax: +33-2-47345142
E-mail: philippe.prene@cea.fr
[b] Laboratoire de Chimie de la Matière Condensée, Université P. & M. Curie,
4 place Jussieu, 75252 Paris Cedex 05, France

in this way. For photovoltaic applications the anatase phase is commonly used. But recently, the first liquid dye-sensitized solar cells using brookite as the n-semiconductor material were reported with promising results.[11]

In the present work, the stable colloidal brookite sol synthesis proposed by Pottier et al.[10] has been optimized in order to control nanoparticle size (diameter from 10 to 20 nm) and to provide a homogeneous coating by the spin-coating technique. The aim of this paper is to evaluate the performances of all-solid-state dye-sensitized solar cells based on Ru-based complexes as the dye and regioregular poly(3-octylthiophene) as the hole conductor. In particular, we are focusing on the TiO_2 mesoporous n-semiconductor film structure and texture. Then we will study the influence of the titania crystalline phase (anatase from Solaronix SA Co. as reference and brookite), nanoparticle size and processing parameters such as the TiO_2-film sintering temperature.

Results and Discussion

1. Characterization of Brookite Colloidal Material

1.1. Thermolysis of $TiCl_4$ in an Acidic Medium

The influence of the synthetic route on the brookite nanoparticle size has been studied. For the thermolysis route ([Ti] = 0.42 M, [HCl] = 3.1 M), after 48 h of ageing at 100 °C, TEM micrographs show strongly-aggregated brookite particles with a mean diameter (Ø) of 10 nm (Figure 1, a). The size of the aggregates varies from 30 to 40 nm, in compliance with the results of QELS measurements (Figure 1, b). After one month of thermolysis at 100 °C the mean size of the aggregates does not change significantly (Figure 2, b). However, the mean particle size evaluated from TEM (Figure 2, a) is notably increased (Ø ≈ 16 nm), suggesting that the growth of the early particles has occurred by the Ostwald ripening process. A particle anisotropy enhancement is observed with thermolysis-time duration.

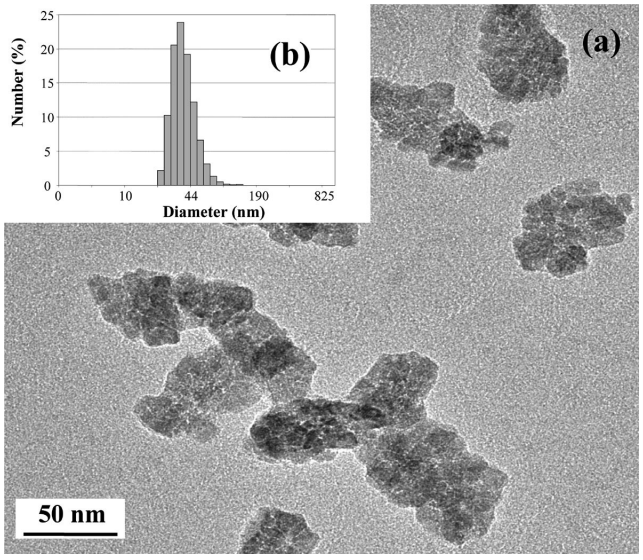

Figure 1. TEM micrograph (a) and hydrodynamic particle-size distribution (b) of the brookite material prepared by the thermolysis route ([$TiCl_4$] = 0.42 M; [HCl] = 3.1 M at 100 °C for 48 h).

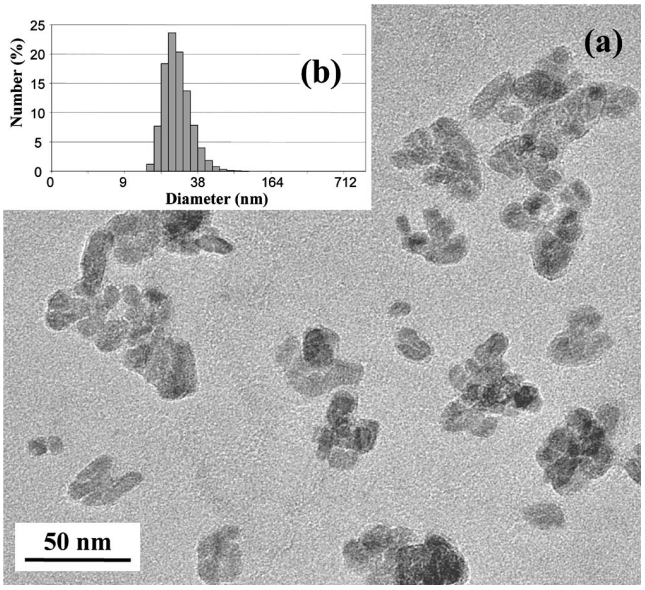

Figure 2. TEM micrograph (a) and hydrodynamic particle-size distribution (b) of the brookite material prepared by the thermolysis route ([$TiCl_4$] = 0.42 M; [HCl] = 3.1 M at 100 °C for one month).

By using the hydrothermal-coupled thermolysis route (see Experimental Section), TEM pictures show aggregated particles (Figure 3, a) with nonhomogeneous particle distribution including two types of particles: quasi-spherical particles (15 nm ≤ Ø ≤ 40 nm) and larger platelets (L = 60 nm and l = 16 nm). The size of the aggregates is in agreement with QELS measurements, which give an object distribution with a mean diameter of about 50 nm (Figure 3, b).

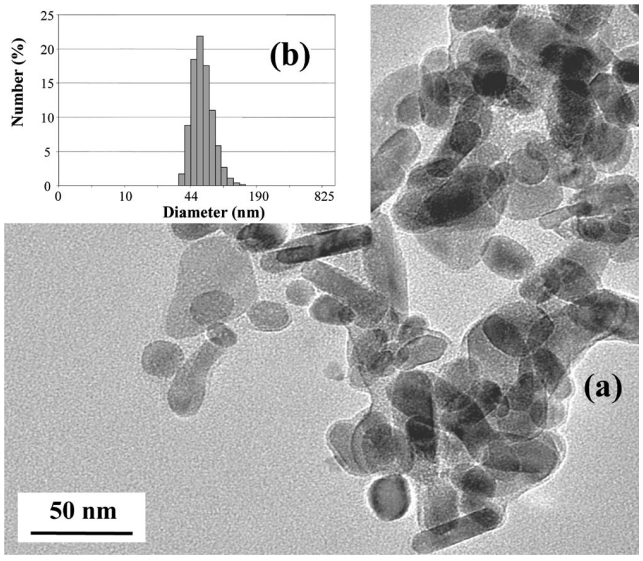

Figure 3. TEM micrograph (a) and hydrodynamic particle-size distribution (b) of the brookite material prepared by the hydrothermal-coupled thermolysis route {[$TiCl_4$] = 0.42 M; [HCl] = 3.1 M at 100 °C for 48 h. and in an autoclave at 220 °C (23×10^5 Pa) for 22 h}.

Whatever the synthetic route and conditions (thermolysis or hydrothermal-coupled thermolysis routes) used, the XRD patterns of TiO_2 powders are characteristic of pure brookite, as shown in Figure 4 for the thermolysis synthesis ([Ti] = 0.42 M, [HCl] = 3.1 M), for one month of ageing at 100 °C. The brookite crystallite sizes ($Ø_C$) estimated from the Scherrer equation applied to the (121) peak are given in Table 1 for the different particle synthetic routes. An increase of crystallite size (from $Ø_C$ = 10 nm to $Ø_C$ = 20 nm) is observed with increasing the thermolysis duration or temperature and pressure ageing conditions (hydrothermal-couple thermolysis route). The brookite crystallite sizes evaluated from the XRD pattern are in accordance with the particle mean diameter determined from TEM observations.

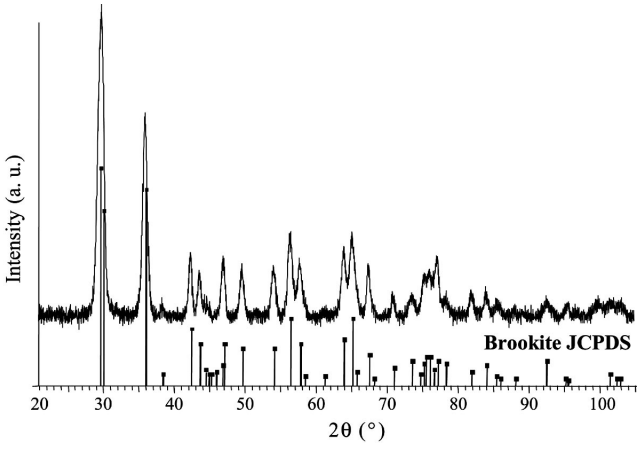

Figure 4. XRD pattern of brookite colloids prepared by the thermolysis route ([$TiCl_4$] = 0.42 M; [HCl] = 3.1 M at 100 °C for one month). The pattern was compared with the brookite JCPDS data.

Table 1. Brookite crystallite size estimated from the Scherrer equation applied to the XRD (121) peak.

Synthetic route	Synthesis conditions	Crystallite size [nm]
Thermolysis	48 h; 100 °C	10
	1 month; 100 °C	14
Hydrothermal-coupled thermolysis	48 h; 100 °C and 22 h; 220 °C (23×10^5 Pa)	20

Well-defined particles of pure brookite have been prepared by the thermolysis and hydrothermal-coupled thermolysis routes. Their mean size is controlled by using Ostwald ripening-based synthetic conditions. Moreover, only one crystalline phase is obtained and the synthetic routes used prevent the brookite to rutile transformation. In this way, the as-prepared brookite nanoparticles are easily peptized in nitric acid solutions and give stable sols that can easily be coated by standard industrial techniques.

1.2. Thermal Stability of TiO_2 Colloids

Typical TGA-TDA curves from investigations of the brookite nanomaterials are represented in Figure 5. The weight loss occurs at three levels, below 200 °C, between 200 and 500 °C and from 500 to 1000 °C. Below 200 °C the weight loss (3.90%) is typical of the elimination of surface-adsorbed molecules. The coupled mass spectrometry (MS) measurements show a single peak, which is characteristic of water. Between 200 and 500 °C the weight loss (2.66%) is attributed to adsorbed water and HNO_3 elimination, in agreement with MS measurements for which NO_2 elimination is observed. Between 500 and 1000 °C the small weight loss (0.76%) associated with an exothermic peak at 865 °C is observed. Such phenomena can be assigned to brookite-to-rutile phase transformation. The TGA-TDA investigations on anatase colloids show anatase-to-rutile phase transformation occurring at 836 °C.

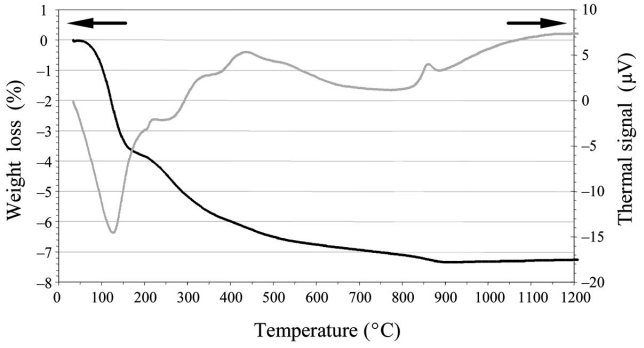

Figure 5. TGA-TDA curves of brookite material prepared by the thermolysis route ([$TiCl_4$] = 0.42 M; [HCl] = 3.1 M at 100 °C for one month). The heating rate is 30 °C min^{-1} in flowing air.

XRD measurements performed on the sintered TiO_2 powders (450 and 600 °C) show that no rutile phase is present after the curing step. In this range of sintering temperature, the brookite and anatase crystalline phases are preserved as observed from the XRD investigations in agreement with the TGA-DTA measurements. The crystallite sizes of brookite and anatase have been estimated for different curing temperatures using the Scherrer equation (Table 2). For the brookite synthetic thermolysis route ([Ti] = 0.42 M, [HCl] = 3.1 M, 100 °C), the crystallite size increases from 10–14 nm at room temperature to 15–17 nm and to 22–23 nm after sintering at 450 °C and 600 °C, respectively. In spite of a larger as-prepared crystallite size ($Ø_C$ = 20 nm), the sintering of brookite prepared by the hydrothermal-coupled thermolysis route leads to a small crystallite size increase ($Ø_C$ = 23 nm), which does not depend on the curing temperature (450 or 600 °C). Moreover, it appears that the 600 °C-sintered brookite powders present a similar crystallite diameter ($Ø_C$ = 23 nm), independent

Table 2. Influence of sintering temperature on brookite and anatase crystallite size.[a]

Crystallite size [nm]	After drying at 20 °C	After sintering at 450 °C	After sintering at 600 °C
	10	15	22
Brookite	14	17	23
	20	24	23
Column 1	14	16	15

[a] Estimated from the Scherrer equation applied to the XRD (121) peak.

of the as-prepared crystallite size and consequently of the liquid medium synthetic route.

On the other hand, the anatase crystallite size is not influenced by the sintering temperature (450 or 600 °C): it remains constant at 14–16 nm.

The XRD results are in accordance with TEM micrograph observations performed on sintered powders (Figure 6). For the brookite thermolysis route and anatase powder, the particle shape does not change notably with sintering temperature, and colloid size distribution seems to remain homogeneous. A significant anisotropy and multimodal diameter distribution are observed for the sintered brookite particles prepared by the hydrothermal-coupled thermolysis route. In all cases, the mean crystallite sizes are close to the corresponding mean particle diameters of the sintered powders.

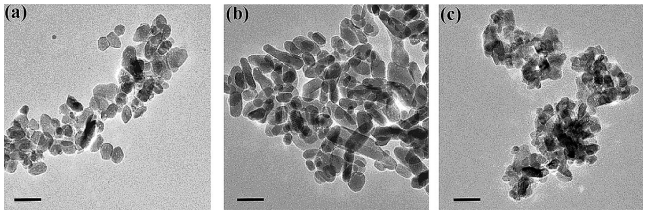

Figure 6. TEM micrographs of powders sintered at 600 °C: (a) brookite particles obtained by thermolysis at 100 °C for one month (b) brookite particles obtained from the autoclave route (c) anatase from Solaronix Co. (common dimension bars: 50 nm).

The textural characteristics of the brookite and anatase powders as a function of sintering temperature are given in Table 3. For both brookite (prepared by the thermolysis and hydrothermal-coupled thermolysis route) and anatase, the surface areas decrease when the sintering temperature increases from 450 to 600 °C and no significant pore volume decrease is observed. With regard to the pore-size deduced from the BJH analyses applied on the BET measurements, the results show a thermolysis-route brookite material pore coarsening with the sintering temperature increase. The pore diameter of anatase and brookite powders prepared by the hydrothermal-coupled thermolysis route remains constant.

Table 3. Influence of sintering temperature on the texture of the TiO_2 material.

TiO_2 powders as-prepared (crystallite size)	Sintering temp. [°C]	Surface area [$m^2 g^{-1}$]	Pore volume [$cm^3 g^{-1}$]	Pore diameter [nm]
Brookite	450	77 ± 3	0.30 ± 0.02	11.1 ± 0.4
($Ø_C$ = 10 nm)	600	53 ± 2	0.26 ± 0.02	13.3 ± 0.4
Brookite	450	76 ± 1	0.21 ± 0.02	7.5 ± 0.3
($Ø_C$ = 14 nm)	600	43 ± 1	0.18 ± 0.02	12.0 ± 0.4
Brookite	450	69 ± 5	0.31 ± 0.03	17.1 ± 1.5
($Ø_C$ = 20 nm)	600	65 ± 5	0.33 ± 0.03	17.7 ± 1.5
Anatase	450	82 ± 1	0.23 ±0.02	8.5 ± 0.3
($Ø_C$ = 14 nm)	600	64 ± 3	0.20 ±0.02	8.6 ± 0.3

A correlation of the XRD and TEM investigations gives rise to a relationship between the grain size and pore diameter changes with sintering temperature. For anatase powders, the observed surface area decreases while the mean particle size is maintained: this obvious contradiction could be explained by the changes in the pore surface properties with the differing sintering temperatures. For the thermolysis-route brookite powders, the pore diameter coarsening and the surface area decrease could have their origin in the crystallite size increase on sintering. The material texture characteristics of the brookite prepared by the hydrothermal-coupled thermolysis route remain constant with the curing temperature, which is related to the small crystallite size increase deduced from the XRD and TEM investigations.

On the other hand, different pore diameters are found (11.1 ± 0.4 and 7.5 ± 0.3 nm for brookite, 8.5 ± 0.3 nm for anatase at 450 °C) for very similar mean particle sizes (15–17 nm). Besides the surface properties, the difference between the brookite and anatase pore diameters could be due to an effect of particle size distribution and brookite colloid shape anisotropy. With regard to the TEM observations and adsorption–desorption isotherm hysteresis shape (Figure 7), the particle distributions seem to be more irregular for brookite than for the anatase samples. Indeed, the Kelvin model approximations used to estimate pore diameter are based on regular pore geometry and do not integrate complex pore shape induced by large particle size distribution and colloid anisotropy.[12]

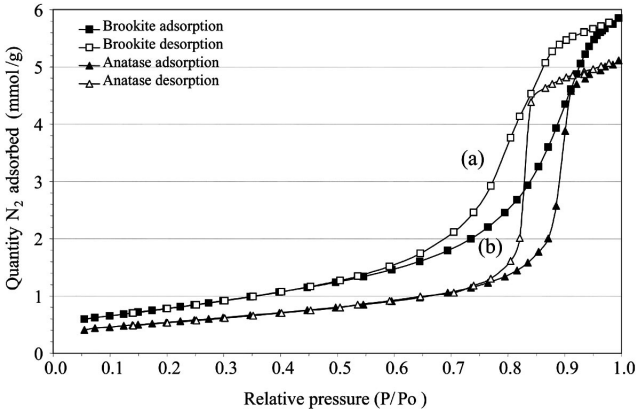

Figure 7. Adsorption–desorption isotherms for powders sintered at 600 °C: (a) brookite (square) obtained by the thermolysis route (at 100 °C for one month) and (b) anatase (triangle) from Solaronix.

2. Investigation of the All-Solid-State Hybrid Solar Cells

2.1. Influence of Sintering Temperature on SnO_2:F Electrode Conductivity

SnO_2:F glasses were fired at 450, 500 and 600 °C at a rate of 30 °C min^{-1} in air to study the influence of the heat-treatment temperature on the SnO_2:F-electrode conduction properties. Figure 8 shows that a temperature increase (from 450 to 600 °C) leads to a slight rise in the SnO_2:F resistivity from 6.58×10^{-4} to 7.73×10^{-4} Ω cm^{-1} because of the insertion of interstitial oxygen atoms during the sintering step under air.[13] The loss in the charge conductor

number is induced by the increase in the annealing temperature, but it is compensated by the improved mobility of the charge conductors in the SnO_2:F-electrode (Figure 9). Thus, the mobility exhibits a jump between 450 and 500 °C because of the combination of a decrease in carrier concentration and an improvement in the purity of the SnO_2 matrix induced by removing defaults from the annealing treatment. These opposed effects compensate each other and the annealing temperature does not impact on the global SnO_2:F-film conductive properties. Consequently the SnO_2:F film can be considered as a good conducting transparent electrode for our TiO_2-sintering temperature range of interest (450 to 600 °C).

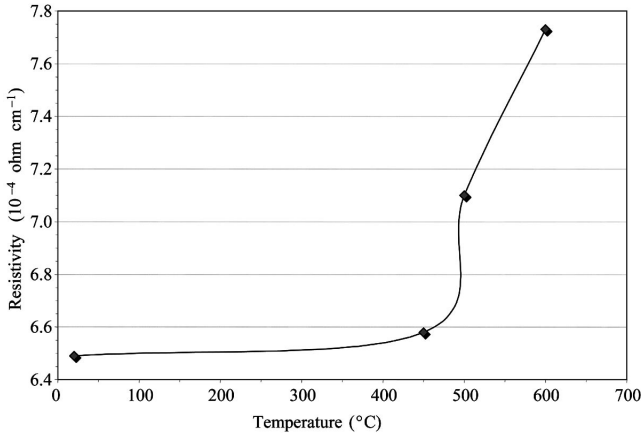

Figure 8. SnO_2:F-film resistivity as a function of sintering temperature (thickness of 1 μm).

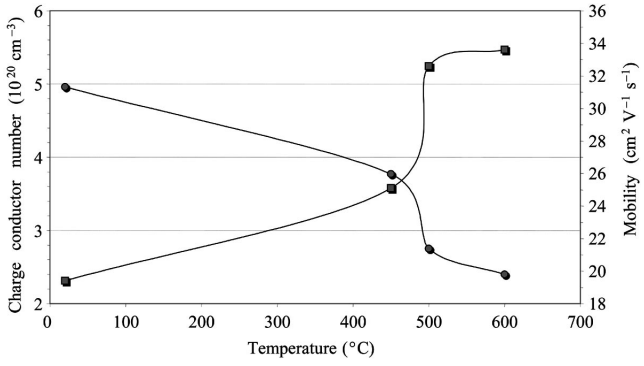

Figure 9. Hall effect characteristics of SnO_2:F electrode: charge conductor numbers (circles) and charge mobility (squares) for different sintering temperatures.

2.2. Influence of the As-prepared Brookite Particle Size on Energy Conversion Efficiency

In all cases, the brookite and anatase powders are clearly stable under heat treatment in air with sintering temperatures between 450 and 600 °C. It is worth noting that film uniformity was maintained upon heating. Crack-free and transparent mesoporous TiO_2 films were thus obtained.

Figure 10 shows the current-voltage (*I-V*) characteristics of the all-solid-state hybrid solar cells based on brookite layers with different initial crystallite sizes ($Ø_C$ = 10, 14 and 20 nm): the same device preparation process has been applied (porous brookite-layer sintering at 600 °C and single organic polymer impregnation) and the TiO_2-film thickness is the same i.e. 500 nm. A decrease in the open circuit voltage (V_{oc}) and the fill factor (*FF*) parameters is observed with an initial particle size increase. However, a significant enhancement of the short circuit current (I_{sc}) is obtained for the 14 nm-as-prepared crystallite size, involving an optimization of the energy conversion efficiency (η_e = 0.48 ± 0.04%). Previously, it has been shown that the 600 °C-sintered brookite crystallite mean size is independent ($Ø_C$ = 22–23 nm) of the size before curing ($Ø_C$ = 10, 14 and 20 nm). The lower overall efficiency level for 10 nm-colloid-based photovoltaic devices could be explained by a higher grain-boundary density inside the porous material. Indeed, the electron conduction properties of the colloid inside the shell are different from those of the core and do not promote electrical conduction between particles in the mesoporous brookite electrode. In the case of a larger initial particle size ($Ø_C$ = 20 nm), the energy conversion efficiency drop is observed. In this case, the particle growth by Ostwald ripening has been performed using the hydrothermal-coupled thermolysis route i.e. at high temperature and pressure (220 °C and 23×10^5 Pa, respectively). Besides the textural brookite-material property changes (widening of crystallite size distribution, more heterogeneous colloid morphology), the synthetic route probably has an influence on the state of the nanoparticle surface properties and the ability of brookite colloids to form the grain-boundary network under sintering conditions. Using the hydrothermal-coupled thermolysis route, the intrinsic electron conductivity in nanoporous brookite material is clearly not promoted.

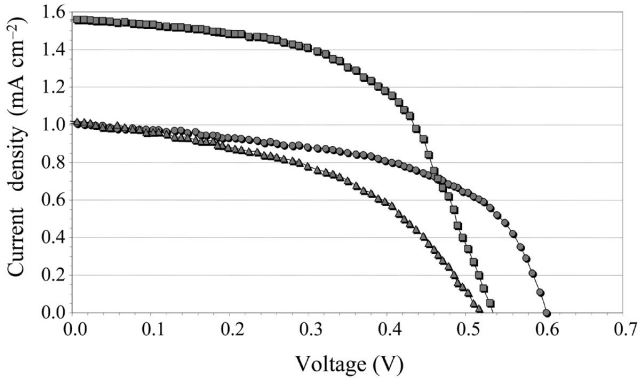

Figure 10. Current-voltage characteristics of the all-solid-state hybrid solar cells prepared by the 600 °C-sintered brookite layer (thickness: 500 nm) with different as-prepared crystallite sizes: 10 nm (circles), 14 nm (squares) and 20 nm (triangles).

2.3. Influence of TiO_2-Sintering on Energy Conversion Efficiency

The *I-V* characteristics of the all-solid state hybrid solar cells prepared by 450 °C- and 600 °C-sintered brookite-films are compared in Figure 11 by plotting the *I-V* characteristics (as-prepared particle size: $Ø_C$ = 14 nm). The char-

acteristic values (V_{oc}, I_{sc} and *FF*) are 0.59 V, 0.55 mA cm^{-2} and 58%, respectively, for a 450 °C-curing temperature, yielding an overall efficiency of 0.19 ± 0.02% at AM 1.5 illumination (1 sun). For the 600 °C-sintered brookite-films an open circuit voltage of 0.53 V, short circuit currents of up to 1.5 mA cm^{-2} and a fill factor of 57% are obtained, with an associated energy conversion efficiency of 0.48 ± 0.04% under standard AM 1.5 conditions.

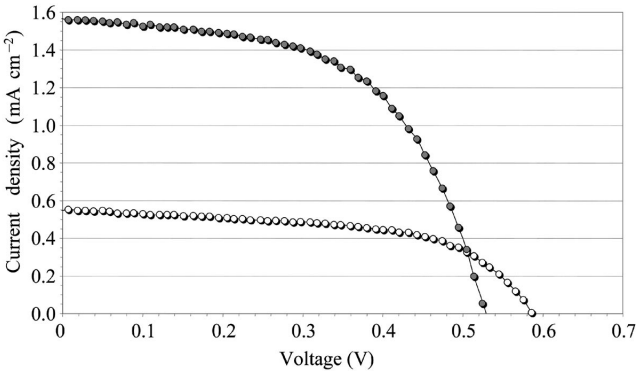

Figure 11. A current-voltage characteristics comparison of the all-solid-state hybrid solar cells based on the brookite-layer (thickness 500 nm) sintered at 450 °C (open circles) and 600 °C (solid circles).

Figure 12 shows the *I-V* plots of the all-solid-state hybrid solar cells based on 450 °C- and 600 °C-sintered anatase films. For a 450 °C-densification temperature, the characteristic values are V_{oc} = 0.43 V, I_{sc} = 2.01 mA cm^{-2} and *FF* = 42%. For the 600 °C-sintered anatase films, V_{oc}, I_{sc} and *FF* are 0.54 V, 2.59 mA cm^{-2} and 54%, respectively. The anatase-based hybrid solar cells present an overall energy conversion efficiency of 0.36 ± 0.03% and 0.74 ± 0.05% under AM 1.5 illumination, for 450 °C- and 600 °C-densification temperatures, respectively.

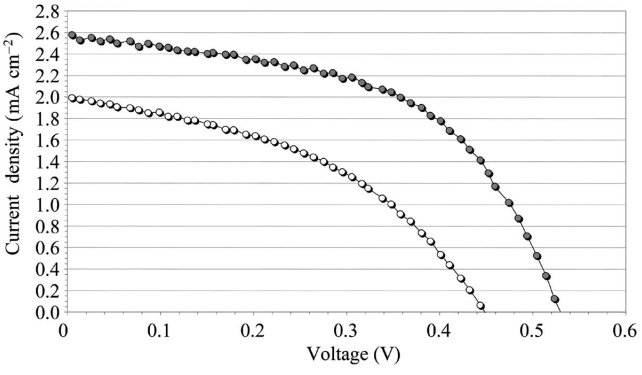

Figure 12. A current-voltage plot comparison of the all-solid-state hybrid solar cells based on the anatase layer (thickness 500 nm) sintered at 450 °C (open circles) and 600 °C (solid circles).

The photovoltaic cell performances (energy conversion efficiency) and the textural and structural characteristics of the TiO_2 electrodes (brookite and anatase) are summarized in Table 4 for comparison. The results are given for the similar as-prepared particle size ($Ø_C$ = 14 nm) and for the same hybrid solar-cell fabrication process [similar mesoporous TiO_2-film thickness (around 500 nm) and a single organic polymer impregnation].

In both cases (anatase and brookite), an increase of the porous TiO_2-film sintering temperature from 450 to 600 °C induces a rise in the energy conversion efficiency, mainly coming from an I_{sc} enhancement. However, the energy conversion efficiency is systematically lower for brookite-based cells than for anatase-based ones, whatever the TiO_2-electrode curing temperature was.

Such cell performance differences can not only be explained by the intrinsic property differences between the anatase and brookite crystalline phases, especially since the bandgap values are very close (ca. 3.2 eV).[14] The textural properties of the porous TiO_2 films such as surface area and pore volume are of the same order of magnitude (<100 m^2 g^{-1} and around 0.2 cm^3 g^{-1}, respectively, Table 4) for anatase and brookite materials. The main difference is the sintering behaviour of the TiO_2 material: a significant growth of the brookite crystallite size (from 14 to 23 nm) after 600 °C sintering has been observed while the anatase nanoparticle diameter remains about constant (from 14 to 15 nm). In the case of brookite material, the ratio of the particle shell part (evaluated to 60%) is greater than the core one. Consequently, the grain boundary has a preponderant influence on the mesoporous TiO_2 properties and on the surface structural properties of the nanoparticles (crystalline state, density of surface defects). Particularly, it impacts on the effective means of electron conduction between nanoparticles, and on the ability of the dye to inject electrons into the TiO_2 network. Moreover, further characterizations (mesoporous TiO_2-layer electrical conductivity, grain-boundary structural characterizations) are needed to understand the phenomena and to enhance the solar cell conversion efficiency.

To the best of our knowledge, it is the first time that brookite-based all-solid-state dye-sensitized solar cells are investigated. Their performances (η_e = 0.48%) are interesting in comparison with all-solid-state polythiophene based cells. But for the 500-nm-photoactive layer they remain lower than the equivalent anatase-based cells (η_e = 0.74%).

Table 4. Comparison of textural and structural characteristics between brookite and anatase, and the energy conversion efficiency of the corresponding solar cells.

	Brookite		Anatase	
Sintering temp. [°C]	450	600	450	600
Crystallite size [nm]	17	23	16	15
Surface area [m^2 g^{-1}]	76 ± 1	43 ± 1	82 ± 1	64 ± 3
Pore volume [cm^3 g^{-1}]	0.21 ± 0.02	0.18 ± 0.02	0.23 ± 0.02	0.20 ± 0.02
Efficiency η_e [%]	0.19 ± 0.02	0.48 ± 0.04	0.36 ± 0.03	0.74 ± 0.05

Conclusions

Mesoporous brookite-TiO_2 thin coatings with different initial particle size have been successfully prepared by a sol-gel process. Crack-free TiO_2 films made of pure brookite nanoparticle structures have been used as n-semiconductor layers in the investigation of all-solid-state dye-sensitized hybrid solar cells with high energy conversion efficiency. Increasing the TiO_2-film sintering temperature from 450 to 600 °C enables the energy conversion efficiency to be enhanced twofold, because of a significantly enhanced current density. High performances (η_e = 0.74%) have been achieved with anatase and P3OT-based hybrid solar cells (600 °C-sintered TiO_2 film thickness of 500 nm). An optimum of conversion efficiency has been reached (η_e = 0.48%) for the as-prepared 14 nm-sized brookite colloid using the same photovoltaic-device fabrication process. This difference probably results from the significant influence of the shell ratio in the brookite material coming from sintering-induced particle growth. It leads to intrinsic property changes and the grain boundary quality impacting on the effective ways of electron conduction between nanoparticles in the porous TiO_2 electrode.

Experimental Section

The anhydrous titanium tetrachloride (i.e., $TiCl_4$) and the regioregular poly(3-octylthiophene) (P3OT, M_w ca. 142000, conductivity: 10^{-6} S cm^{-1}) were obtained from Aldrich and used as received. The Ru-based complex dye (II) [RuL2(NCS)2:2 TBA, i.e. *cis*-bis(isothiocyanato)bis(2,2′-bipyridyl-4,4′-dicarboxylato)ruthenium] was provided by Solaronix SA Co.

Synthesis of Brookite Colloids: Two routes have been used to prepare the brookite nanoparticles: a thermolysis route and a hydrothermal-coupled thermolysis one. The first preparation route consists of the synthesis of brookite colloids by the thermolysis of $TiCl_4$ in a concentrated hydrochloric acid solution (HCl). TiO_2 particles were formed by adding pure $TiCl_4$ dropwise to a HCl medium (3.1 M). The final titanium concentration in the mixture was 0.42 M. The solution was heated and maintained at 100 °C in an oven. After ageing, the solid was centrifuged and washed with distilled water. At this stage the mixture was composed of brookite and rutile naonoparticles. The difference in size of both crystalline phases allows a selective peptization of brookite in a nitric acid medium (HNO_3).[10] The solid that was collected after distilled-water washing was treated with a HNO_3 solution (3 M) for ca. 30 min. The suspension was again centrifuged and the recovered solid phase was dispersed twice in water. The pH of the final sol was around 1.5.

For the hydrothermal-coupled thermolysis route, thermolysis ageing of $TiCl_4$ in concentrated HCl was fixed for 48 h at 100 °C. The necessary steps to isolate brookite from rutile were performed. Then, the aqueous brookite sol was diluted in a HNO_3 (0.1 M) solution ([TiO_2] = 0.2 M) and subjected to a hydrothermal Ostwald ripening for 22 h at 220 °C in an autoclave (23×10^5 Pa). The solid collected after centrifugation was treated with a HNO_3 solution (3 M) at reflux for 15 h. The recovered solid phase was dispersed in water as previously (pH ≈ 2).

In all cases, the TiO_2 solution was concentrated ([TiO_2] = 10% wt) and dialyzed in distilled water until pH = 2. The TiO_2 solution was concentrated again ([TiO_2] = 20% wt) and diluted in methanol (MeOH; 1:1 wt).

TiO_2 Electrode Preparation: The 500-nm-thick mesoporous films of anatase or brookite-synthesized TiO_2 were deposited onto the working electrode consisting of a stack of a dense TiO_2 layer and a conducting fluorine-doped tin oxide SnO_2:F electrode covered glass substrate. Brookite-TiO_2 films were spin-coated (2.000 rpm) from the colloidal sol (10 wt.-% TiO_2 in H_2O:MeOH = 1:1, wt.). Anatase-TiO_2 layers were also prepared by spin-coating (1000 rpm) from a paste provided by Solaronix SA Co. dissolved in ethanol (EtOH). In both cases, TiO_2 films were sintered at 450 or 600 °C (ramp of 30 °C min^{-1}) for 30 min.

Solid State Hybrid Solar Cell Fabrication: After the curing step, the mesoporous TiO_2 films were dye-functionalized by soaking them for 24 h in a solution of $RuL_2(NCS)_2$:2 TBA dye (5×10^{-4} M) in dry ethanol at room temperature in the dark. The hole-transport layer was immediately spin-coated (500 rpm) from a P3OT solution in toluene (30 g L^{-1}). Finally, a 300-nm-thick gold back electrode was deposited onto the organic semiconductor film by sputtering. The thickness of the hole-conducting polymer on top of the TiO_2 was typically in the range of 200–300 nm, as determined by Dektak profilometer measurements.

Characterization Techniques: For the TiO_2 nanoparticle characterizations, the X-ray diffraction patterns (XRD) were performed with a D500 powder diffractometer operating in the reflection mode with monochromatized Co-K_α radiation (λ = 1.79026 Å). The crystallite size ($Ø_C$) was estimated by applying the Scherrer equation to the full width at half maximum (FWHM) of the (121) and (110) peak for brookite and anatase, respectively. TiO_2 powders were obtained by drying TiO_2 sols at room temperature. Transmission electronic microscopy (TEM) was carried out with a Philips CM 20 instrument (200 kV) coupled with a CCD Gatan camera. Samples were prepared by evaporating very dilute sols of the prepared samples or sintered powders onto carbon-coated grids. Measurements of quasi-elastic light scattering (QELS) were performed on stable suspensions (10^{-1} g L^{-1}) using a Malvern instrument equipped with a He-Ne laser. A SETRAM TAG24–1600 was used for TGA-TDA measurements. Samples of powder (50 mg) were obtained from the colloidal sol by drying at room temperature and were put into an Al_2O_3 crucible. The heating rate was 30 °C min^{-1} in flowing air. The recorded temperature range was from room temperature to 1200 °C. Brunauer–Emmett–Teller (BET) measurements were performed with a Tristar 3000 apparatus. Powders were previously degassed for 8 h at room temperature under vacuum.

For the conducting fluorine-doped tin oxide SnO_2:F electrode, the resistivity (ρ), the mobility (μ) and the carrier concentrations (N) were measured with a commercial Biorad system (HC 5500PC), using the Van Der Pauw method.

For the solid hybrid solar cell performance characterizations, the current-voltage (I-V) characteristics were measured with a Solaronix SA Co. light source solar simulator using a xenon light source that was focused to give 1000 W m^{-2}, the equivalent of one sun at standard air mass (AM) 1.5 conditions. To test the reproducibility of the results, each measurement was made simultaneously on five identical prototype cells. The devices were not sealed or otherwise protected. The illuminated active area was 0.25 cm^2.

Acknowledgments

We thank D. Jalabert of the University of Orleans for the TEM micrographs.

[1] B. O'Regan, M. Grätzel, *Nature* **1991**, *353*, 737–740.
[2] a) M. K. Nazeeruddin, A. Kay, I. Rodicio, R. Humphry-Baker, E. Müller, P. Liska, N. Vlachopoulos, M. Grätzel, *J. Am. Chem. Soc.* **1993**, *115*, 6382–6390; b) M. Grätzel, *J. Photochem. Photobiol., A* **2004**, *164*, 3–14.
[3] P. Wang, S. M. Zakeeruddin, J. E. Moser, R. Humphry-Baker, P. Comte, V. Aranyos, A. Hagfeldt, M. K. Nazeeruddin, M. Grätzel, *Adv. Mater.* **2004**, *16*, 1806–1811.
[4] a) Q. B. Meng, K. Takahashi, X. T. Zhang, I. Sutanto, T. N. Rao, O. Sato, A. Fujishima, *Langmuir* **2003**, *19*, 3572–3574; b) B. O'Regan, F. Lenzmann, R. Muis, J. Wienke, *Chem. Mater.* **2002**, *14*, 5023–5029.
[5] A. F. Nogueira, C. Longo, M. A. De Paoli, *Coord. Chem. Rev.* **2004**, *248*, 1455–1468.
[6] a) J. Krüger, R. Plass, L. Cevey, M. Piccirelli, M. Grätzel, *Appl. Phys. Lett.* **2001**, *79*, 2085–2087; b) B. O'Regan, D. T. Schwartz, S. M. Zakeeruddin, M. Grätzel, *Adv. Mater.* **2000**, *12*, 1263–1267; c) L. H. Slooff, M. M. Wienk, J. M. Kroon, *Thin Solid Films* **2004**, *451–452*, 634–638; d) C. Y. Kwong, A. B. Djurisic, P. C. Chui, K. W. Cheng, W. K. Chan, *Chem. Phys. Lett.* **2004**, *384*, 372–375; e) G. R. A. Kumara, A. Konno, K. Shiratsuchi, J. Tsukahara, K. Tennakone, *Chem. Mater.* **2002**, *14*, 954–955; f) K. Tennakone, G. R. A. Kumara, A. R. Kumarasinghe, K. G. U. Wijayantha, P. M. Sirimanne, *Sci. Technol.* **1995**, *10*, 1689–1693; g) K. Tennakone, G. R. A. Kumara, I. R. M. Kottegoda, K. G. U. Wijayantha, V. P. S. Perera, *J. Phys. D Appl. Phys.* **1998**, *31*, 1492–1496; h) B. O'Regan, D. T. Schwartz, *Chem. Mater.* **1995**, *7*, 1349–1354; i) J. Hagen, W. Schaffrath, P. Otschik, R. Fink, A. Bacher, H.-W. Schmidt, D. Haarer, *Synth. Met.* **1997**, *89*, 215–220; j) P. Ravirajan, D. D. C. Bradley, J. Nelson, S. A. Haque, J. R. Durrant, H. J. P. Smit, J. M. Kroon, *Appl. Phys. Lett.* **2005**, *86*, 143101; k) D. Gebeyehu, C. J. Brabec, N. S. Sariciftci, *Thin Solid Films* **2002**, *403–404*, 271–274; l) C. L. Huisman, A. Goossens, J. Schoonman, *Synth. Met.* **2003**, *138*, 237–241; m) C. D. Grant, A. M. Schwartzberg, G. P. Smestad, J. Kowalik, L. M. Tolbert, J. Z. Zhang, *J. Electroanal. Chem.* **2002**, *522*, 40–48; n) C. D. Grant, A. M. Scwartzberg, G. P. Smestad, J. Kowalik, L. M. Tolbert, J. Z. Zhang, *Synth. Met.* **2003**, *132*, 197–204; o) S. Spiekermann, G. Smestad, J. Kowalik, L. M. Tolbert, M. Grätzel, *Synth. Met.* **2001**, *121*, 1603–1604; p) D. Gebeyehu, C. J. Brabec, N. S. Sariciftci, D. Vangeneugden, R. Kiebooms, D. Vanderzande, F. Kienberger, H. Schindler, *Synth. Met.* **2002**, *125*, 279–287; q) C. Zafer, C. Karapire, N. S. Sariciftci, S. Icli, *Sol. Energy Mater. Sol. Cells* **2005**, *88*, 11–21; r) K. M. Coakley, M. D. McGehee, *Appl. Phys. Lett.* **2003**, *83*, 3380–3382; s) K. M. Coakley, M. D. McGehee, *Chem. Mater.* **2004**, *16*, 4533–4542; t) Q. Fan, B. McQuillin, D. D. C. Bradley, S. Whitelegg, A. B. Seddon, *Chem. Phys. Lett.* **2000**, *347*, 325–330; u) P. M. Sirimanne, T. Shirata, L. Damodare, Y. Hayashi, T. Soga, T. Jimbo, *Sol. Energy Mater. Sol. Cells* **2003**, *77*, 15–24; v) L. B. Roberson, M. A. Poggi, J. Kowalik, G. P. Smestad, L. A. Bottomley, L. M. Tolbert, *Coord. Chem. Rev.* **2004**, *248*, 1491–1499; w) A. J. Breeze, Z. Schlesinger, S. A. Carter, P. J. Brock, *Phys. Rev. B* **2001**, *64*, 125205; x) P. A. van Hal, M. M. Wienk, J. M. Kroon, W. J. Verhees, L. H. Sloof, J. H. van Gennip, P. Jonkheijm, R. A. J. Janssen, *Adv. Mater.* **2003**, *15*, 118–121; y) M. Y. Song, K. J. Kim, D. Y. Kim, *Sol. Energy Mater. Sol. Cells* **2005**, *85*, 31–39.
[7] a) J. Krüger, R. Plass, M. Gratzel, H. J. Matthieu, *Appl. Phys. Lett.* **2002**, *81*, 367–369; b) Q. B. Meng, K. Takahashi, X. T. Zhang, I. Sutanto, T. N. Rao, O. Sato, A. Fujishima, *Langmuir* **2003**, *19*, 3572–3574.
[8] a) U. Bach, D. Lupo, P. Comte, J. E. Moser, F. Weissörtel, J. Salbeck, H. Spreitzer, M. Grätzel, *Nature* **1998**, *395*, 583–585; b) E. Lancelle-Beltran, Ph. Prené, C. Boscher, Ph. Belleville, P. Buvat, C. Sanchez, *Adv. Mater.* **2006**, *18*, 2579–2582; c) E. Lancelle-Beltran, Ph. Prené, C. Boscher, Ph. Belleville, P. Buvat, S. Lambert, F. Guillet, C. Boissière, D. Grosso, C. Sanchez, *Chem. Mater.* **2006**, *18*, 6152–6156.
[9] M. Koelsch, S. Cassaignon, C. T. Thanh Minh, J. F. Guillemoles, J. P. Jolivet, *Thin Solid Films* **2004**, *451–452*, 86–92.
[10] A. Pottier, C. Chanéac, E. Tronc, L. Mazerolles, J. P. Jolivet, *J. Mater. Chem.* **2001**, *11*, 1116–1121.
[11] a) *US Pat.*, 6 300 559, **2001**; b) K. J. Jiang, T. Kitamura, H. Yin, S. Ito, S. Yanagida, *Chem. Lett.* **2002**, *31*, 872–873.
[12] F. Rouquerol, J. Rouquerol, K. Sing in *Adsorption by powders & porous solids. Principles, methodology and applications*, Academic press, London, **1999**.
[13] a) E. Shanti, A. Banerjee, K. L. Chopra, *Thin Solid Films* **1982**, *88*, 93–100; b) K. H. Yoon, J. S. Song, *Thin Solid Films* **1993**, *224*, 203–208; c) K. L. Chopra, S. Major, D. K. Pandya, *Thin Solid Films* **1983**, *102*, 1–46.
[14] M. Koelsch, S. Cassaignon, J. F. Guillemoles, J. P. Jolivet, *Thin Solid Films* **2002**, *403–404*, 312–319.

Received: September 24, 2007
Published Online: January 25, 2008

